PAPER • OPEN ACCESS

Analysis and expansion of the quasi-continuous exhaust (QCE) regime in ASDEX Upgrade

View the article online for updates and enhancements.

Analysis and expansion of the quasi-continuous exhaust (QCE) regime in ASDEX Upgrade

M. Faitsch[1,*] , **T. Eich**[1] , **G.F. Harrer**[2] , **E. Wolfrum**[1] , **D. Brida**[1] , **P. David**[1] , **M. Dunne**[1] , **L. Gil**[3] , **B. Labit**[4] , **U. Stroth**[1,5] , **the ASDEX Upgrade Team**[a] **and the EUROfusion MST1 Team**[b]

[1] Max-Planck-Institute for Plasma Physics, Boltzmannstr. 2, D-85748 Garching, Germany
[2] Institute of Applied Physics, TU Wien, Fusion@ÖAW, Wiedner Hauptstr. 8-10, 1040 Vienna, Austria
[3] Instituto de Plasmas e Fusão Nuclear, Instituto Superior Técnico, Universidade de Lisboa, 1049-001 Lisboa, Portugal
[4] Ecole Polytechnique Federale de Lausanne, Swiss Plasma Center, CH-1015 Lausanne, Switzerland
[5] Physik Department E28, Technische Universität München, 85748 Garching, Germany

E-mail: Michael.Faitsch@ipp.mpg.de

CrossMark

Abstract

The quasi-continuous exhaust (QCE) regime, formerly known as either type-II ELM or small ELM regime is studied in ASDEX Upgrade. The regime is a natural type-I ELM-free H-mode. The operational space of QCE discharges in ASDEX Upgrade with respect to their separatrix conditions and their power exhaust capabilities are presented. A significant broadening of the power fall-off length is observed, correlating to an increased separatrix density and pressure. Moreover, the possible reactor relevance of this regime is demonstrated by expanding the operational space to low edge safety factor and demonstrating the benign tungsten impurity behaviour. A discharge without any type-I ELM from start to end reaching a partially detached divertor at high normalised energy confinement time is presented.

Keywords: turbulence, separatrix, H-mode, magnetic confinement, QCE

(Some figures may appear in colour only in the online journal)

1. Introduction

Two main challenges of power exhaust for future tokamak power plants are the avoidance of transients, like type-I ELMs, and access to a (partially) detached divertor. These two constraints are often studied independently of each other. Many type-I ELM avoidance schemes focus on a low pedestal top collisionality which will be present in a future reactor due to the high temperature. The access to a detached regime requires a high pedestal foot—or separatrix—collisionality due to the required high density. While present day tokamak experiments can approach reactor-like values for either independently, the combination of both is only possible with a reactor-sized experiment.

A promising regime in which the absence of type-I ELMs is linked to the tailoring of the pedestal profile at the foot is the so-called quasi-continuous exhaust (QCE) regime. The regime is a natural type-I ELM-free H-mode that was previously

---

identified with type-II ELMs [1–5] or small ELMs [6, 7] and is now named QCE [8] due to enhanced filamentary transport at the plasma edge compared to inter-type-I ELM phases. While in ASDEX Upgrade this regime is achieved with high normalised energy confinement time when using highly shaped plasma discharges at high separatrix density [6], also plasmas with low plasma shaping and high separatrix density can be type-I ELM-free. The EDA H-mode [9] is another ELM-free regime observed at ASDEX Upgrade with high plasma shaping [10]. The EDA H-mode is situated at lower powers and separatrix densities, with generally better energy confinement compared to QCE, but with re-occurrence of ELMs above a separatrix power threshold. At lower fuelling and separatrix density a transition from the QCE to the EDA H-mode regime is observed. The conditions at the separatrix seem to be important as access condition to a small ELM regime.

The high separatrix density, together with an observed broadening of the power fall-off length [8] is believed to be beneficial for detachment [11, 12]. However, these considerations assume steady-state conditions, while the QCE has temporarily changing heat and particle fluxes caused by the filamentary transport. Future experiments and modelling have to show if these filaments can be detached/buffered in order to achieve time-integrated low particle erosion at the divertor. While it was shown that low amplitude type-III ELMs can be buffered in JET [13], the same was not yet studied for the filaments in the QCE regime.

A theoretical description of the QCE regime is given by ballooning modes being unstable at the pedestal foot, close to the separatrix. These ballooning modes are thought to cause transport, limit the radial extend of the steep gradient region and thereby prevent the occurrence of type-I ELMs [6, 14, 15].

The QCE regime exhibits a density shoulder, likely linked to the filamentary transport across the separatrix [8, 16]. A density shoulder is associated with enhanced particle and heat fluxes to plasma facing components outside the divertor region [17]. Future studies have to show if this will cause an unacceptable heat load and erosion and if so investigate measures to suppress these.

Recent works in ASDEX Upgrade showed that turbulence considerations, similar in nature to the work by [18], outline the separatrix operational space of the H-mode by successfully describing the H-L transition, the L-mode density limit as well as an ideal ballooning limit [19, 20].

In this work we analyse the operational space of QCE discharges in ASDEX Upgrade with respect to their separatrix conditions and their power exhaust capabilities. Moreover, we show the possible reactor relevance of this regime by expanding the operational space to low edge safety factor q_{95}, demonstrating the benign tungsten impurity behaviour, and develop a discharge without any type-I ELM from start to end.

The article is organised as follows: section 2 defines an automatic qualifier to distinguish between type-I ELMs and QCE filaments. Section 3 provides an experimental approach to access the QCE regime by a correlation with engineering as well as physics parameters. The achievable electron

temperature and density range at the separatrix is presented in section 4. In section 5 a scaling of the pressure fall-off length as well as the broadening of the power fall-off length with increasing separatrix density and pressure is discussed. A correlation between edge quantities and confinement is presented in section 6. Section 7 highlights the route to low safety factor and the low tungsten core concentration in QCE. Section 8 presents a discharge avoiding type-I ELMs from start to end. A discussion on ITER-like plasma parameters and the open questions regarding detachment are presented in section 9. Section 10 contains a summary and conclusions.

2. Qualifier for absence of ELMs

For the automated analysis of the operational space of H-mode discharges without type-I ELMs we searched for a qualifier for the absence of ELMs. We inspected many different signals that could act as qualifier in ASDEX Upgrade. The most reliable one proved to be the scrape-off layer current measured via shunts in the divertor tiles I_{SOL}. Type-I ELMs show up as large peaks on a signal that is dominated by thermo currents [21]. Our ELM proxy is defined by the shunt current measured at the outer divertor target. The current is multiplied by the edge safety factor to account for the resistivity varying with connection length. The edge safety factor is defined as [20]

$$q_{cyl} = \frac{B_{tor}}{B_{pol}} \frac{a_{geo}}{R_{geo}} \hat{\kappa} \qquad (1)$$

with

$$B_{pol} = \frac{\mu_0 I_p}{2\pi a_{geo} \hat{\kappa}} \qquad (2)$$

$$\hat{\kappa} = \sqrt{\frac{1 + \kappa^2(1 + 2\delta^2 - 1.2\delta^3)}{2}}. \qquad (3)$$

Here, B_{tor} is the toroidal magnetic field on axis, a_{geo} and R_{geo} are the minor and major radii, κ is the elongation, δ the averaged triangularity, μ_0 the vacuum permeability and I_p the plasma current. We normalise this quantity by dividing it by 21 kA and define it as

$$E_{prox} = \frac{q_{cyl}}{21} |I_{SOL}| (kA). \qquad (4)$$

With this normalisation, E_{prox} is a dimensionless quantity. For a value below 1 the plasma is in the QCE regime, above 2 type-I ELMs are present and in between 1 and 2 the ELM behaviour is ambiguous. Note here, also discharge phases in EDA H-mode are ELM-free and have $E_{prox} < 1$.

In order to show that E_{prox} correlates with the power load on the outer divertor we chose a type-I ELMy discharge and compared E_{prox} with the infrared thermography (IR, [22]) measurements. Figure 1 shows the relation between divertor power load P_{div}^{IR} and E_{prox}. The divertor power load is the spatially integrated heat flux measured by IR. $E_{prox} = 1.0$ corresponds roughly to 2–2.5 MW divertor power load. At higher values,
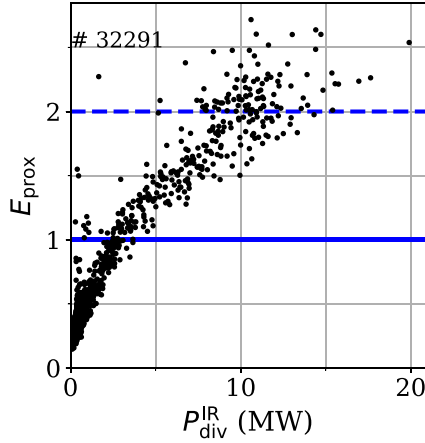
Figure 1. Integrated power load on the outer divertor measured by infrared thermography $P_{\mathrm{div}}^{\mathrm{IR}}$ compared to the ELM proxy E_{prox}. Data is taken from # 32291 in the time interval between 3.4 s and 5.0 s where the discharge was in a clear type-I ELMy H-mode with constant plasma shape. The blue solid (dashed) line represents the upper (lower) limit used for detecting ELM-free (type-I ELMs) time points.

e.g. during type-I ELMs, no strict linear correlation between divertor power load and shunt current exists, however, a larger shunt current still corresponds to larger divertor power load.

In the remainder of this article we distinguish between time windows with type-I ELMs from those with QCE filaments only. For this, the maximum (99.9% percentile) of E_{prox} in an interval is taken. As an example, figure 2 shows three 150 ms time slices of integrated divertor power load and normalised divertor shunt current of a discharge with type-I ELMy and QCE phases. They represent (a) a type-I ELM phase with $\max(E_{\mathrm{prox}}) = 4.1$, (b) a mixed phase with some ELMs with $\max(E_{\mathrm{prox}}) = 2.7$ and (c) a QCE phase with $\max(E_{\mathrm{prox}}) = 0.6$. For the last window, no IR measurements are available due to volume radiation.

We assembled a data set covering a wide range of plasma quantities in ASDEX Upgrade. The main parameters are summarised in table 1. P_{heat} is the applied power corrected for neutral beam shine-through losses and changes in stored energy. The data set is concentrated at high plasma shaping (high upper triangularity of $\delta_{\mathrm{up}} \approx 0.3$, close to double-null). This high plasma shaping is a key ingredient for realising the QCE regime whilst maintaining a high normalised confinement time [1, 14, 15]. Each data point represents an average of around 150 ms. This ensures steady state values and allows the separatrix analysis of Thomson scattering (TS, [23]) data as described in [19, 20] using the sub-script *edge* for the reference point 1 mm (poloidally averaged) inside the separatrix ($\rho_{\mathrm{pol}} \approx 0.999$). This TS analysis provides edge temperature $T_{\mathrm{e,edge}}$, density $n_{\mathrm{e,edge}}$ and pressure $p_{\mathrm{e,edge}}$ as well as the exponential fall-off lengths of these. The data processing is sketched in the following paragraph.

The TS profiles are mapped to the outer mid-plane by the magnetic equilibrium reconstruction. Due to the strong

gradients, the location of the separatrix is chosen by a power balance assuming Spitzer–Härm electron heat conduction being the dominant transport mechanism in the scrape-off layer setting the electron temperature at the separatrix. The temperature is estimated following [24]:

$$T_{\mathrm{e,sep}} \approx \left(\frac{7 P_{\mathrm{SOL}} q_{\mathrm{cyl}}^2 A}{16 \kappa_0^e \hat{\kappa} \langle \lambda_{\mathrm{q}} \rangle} \right)^{\frac{2}{7}} \tag{5}$$

with aspect ratio A and Spitzer–Härm electron heat conduction coefficient κ_0^e. Typically a ratio of $\lambda_{\mathrm{q}} = \frac{2}{7} \lambda_{T_{\mathrm{e}}}$ is used. At low separatrix density the validity of this assumption was shown in ASDEX Upgrade [25–27]. In our QCE data set we account for a change in the electron temperature gradient between inside and outside the separatrix as reported in [8]. Here, we use $\lambda_{\mathrm{q}} = \frac{2}{5} \lambda_{T_{\mathrm{e}}}$, in line with the measurements shown in section 5. Note, this does not mean we do not follow Spitzer–Härm electron heat conduction, but rather that the gradient *just inside*, which dominates the estimate of $\lambda_{T_{\mathrm{e}}}$ in our approach, is steeper than in the near scrape-off layer. We are interested in the gradients and absolute values *just inside* the separatrix.

Figure 3 shows a comparison between two approaches to extract the edge density for the full data set. The edge density from the integrated data analysis (IDA, [28]) is very similar to the values obtained by the technique applied here (using Spitzer–Härm electron heat conduction, SH). On the other hand, the IDA edge temperature scatters significantly making the SH approach necessary.

A manual classification between type-I ELMy and QCE phases is compared to the ELM proxy E_{prox} to validate the automatic sorting for the full data set. Figure 4 shows $\max(E_{\mathrm{prox}})$ as a function of the edge collisionality

$$\nu_{\mathrm{e,edge}}^* = \frac{\pi q_{\mathrm{cyl}} R_{\mathrm{geo}}}{1.03 \cdot 10^{16}} \frac{n_{\mathrm{e,edge}}}{T_{\mathrm{e,edge}}^2} Z_{\mathrm{eff}}. \tag{6}$$

$Z_{\mathrm{eff}} = 1.24$ is assumed for all data points (no discharges with impurity seeding are included). The marker type is a binary classification by hand. It is observed that nearly no type-I ELM phase has $\max(E_{\mathrm{prox}}) < 1$ and nearly no QCE phase has $\max(E_{\mathrm{prox}}) > 2$, while phases in both regimes exist in the space between. The manual classification is less strict than the automatic sorting in the sense that single ELMs within a QCE time window are not marked as ELMy. This is seen in figure 4 with points marked as QCE but having $\max(E_{\mathrm{prox}}) > 2$. In the remainder of the paper, we use the automatic sorting and only phases with $\max(E_{\mathrm{prox}}) < 1$ as QCE and $\max(E_{\mathrm{prox}}) > 2$ as type-I ELMy and discard the phases in between. This binary sorting has two main drawbacks: (i) the drive of the filaments exists already in phases where occasional type-I ELMs are present [6] and (ii) the transition can be a smooth process, with the type-I ELM amplitude reducing continuously until the type-I ELMs vanish completely [8]. Hence, we are not searching the onset point of the filaments but the absence point of type-I ELMs.
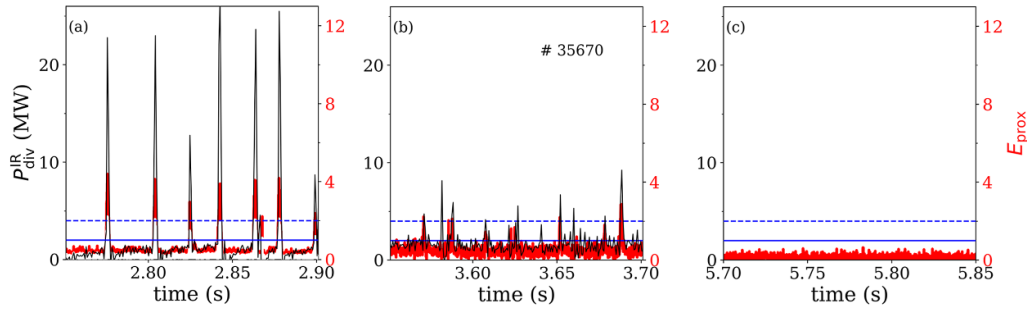
Figure 2. Time traces of divertor power estimated with IR thermography P_{div} and ELM proxy E_{prox} for #35670. (*a*) type-I ELMs are present, (*b*) phase with low amplitude ELMs and filaments, (*c*) QCE phase. The IR data for time interval (*c*) is not reliable due to volume radiation. The blue solid (dashed) line represents the upper (lower) limit used for detecting ELM-free (type-I ELMy) phases.

Table 1. Main parameters of the analysed data set.

# points	# shots	$|B_{\mathrm{tor}}|$ (T)	I_{p} (MA)	q_{95}	κ	δ_{up}	P_{heat} (MW)	$n_{\mathrm{e,edge}}$ ($10^{19}\,\mathrm{m}^{-3}$)
1482	114	1.4–2.8	0.6–1.1	3.3–8.2	1.5–1.9	0.0–0.4	0.1–15	1.2–7.4
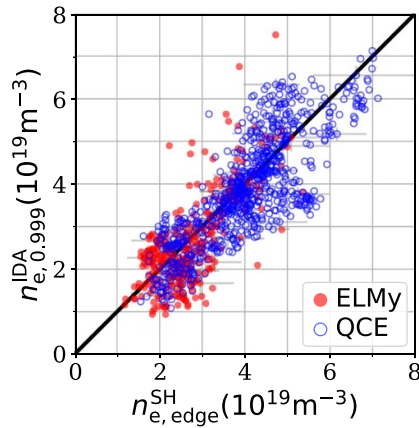
Figure 3. Edge density from the Spitzer–Härm electron heat conduction (SH) approach compared to the value from the integrated data analysis (IDA) at $\rho_{\mathrm{pol}} = 0.999$. Open blue symbols represent QCE phases, filled red symbols represent type-I ELMy phases. Representative error-bars are shown.
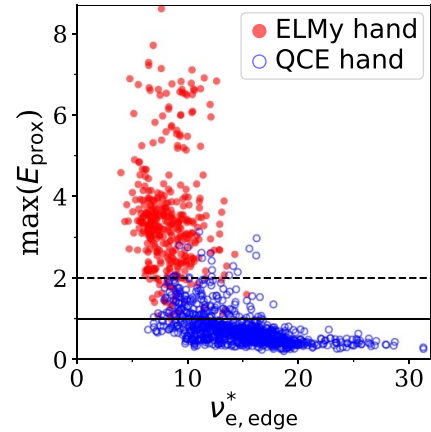
Figure 4. ELM proxy $\max(E_{\mathrm{prox}})$ as a function of edge collisionality $\nu_{\mathrm{e,edge}}^*$. Open blue symbols represent QCE phases, filled red symbols represent type-I ELMy phases as sorted by hand. The black lines represent the threshold for the automatic sorting, with the solid line being the upper limit for QCE and the dashed line the lower limit for type-I ELMy.

3. Access conditions to QCE

For type-I ELMs to be suppressed, transport across the separatrix must be increased so that the pedestal pressure profile cannot reach the global peeling-ballooning stability threshold. Here, we are looking for the conditions that provide the necessary high transport level.

The access conditions to the QCE regime are investigated in two ways. First, we look at engineering parameters, namely edge density $n_{\mathrm{e,edge}}$ and the power crossing the separatrix P_{SOL}. Then, we investigate the access dependence on edge collisionality $\nu_{\mathrm{e,edge}}^*$ and turbulence control parameter α_{t}, both parameters associated with increased transport [29, 30]. Additionally, we investigate the closeness of the separatrix pressure profile to the ideal ballooning limit.

The two engineering parameters for the scrape-off layer of a tokamak, edge density $n_{\mathrm{e,edge}}$ and power crossing the

separatrix P_{SOL}, are shown in figure 5. The power crossing the separatrix is calculated using P_{heat} and subtracting the radiated power inside the confined region as calculated from a bolometric reconstruction [31]. For both parameters, there is a considerable overlap of QCE and type-I ELMy phases. However, it is noted that only QCE phases exist below a ratio of $P_{\mathrm{SOL}}(\mathrm{MW})/n_{\mathrm{e,edge}}(10^{19}\,\mathrm{m}^{-3}) = 1$ and/or above $n_{\mathrm{e,edge}} = 5.4 \cdot 10^{19}\,\mathrm{m}^{-3}$. The power dependence is consistent with findings from non-linear MHD simulations performed with JOREK [32]. These simulations find a transition to type-I ELMs when increasing P_{SOL} starting from a small ELM phase.

Two physics quantities, α_{t} and α_{MHD} (normalised to the ideal ballooning limit α_{crit}), are shown in figure 6. They are defined as in [19]:

$$\alpha_{\mathrm{t}} = \frac{1}{100} q_{\mathrm{cyl}} \cdot \nu_{\mathrm{e,edge}}^* \tag{7}$$
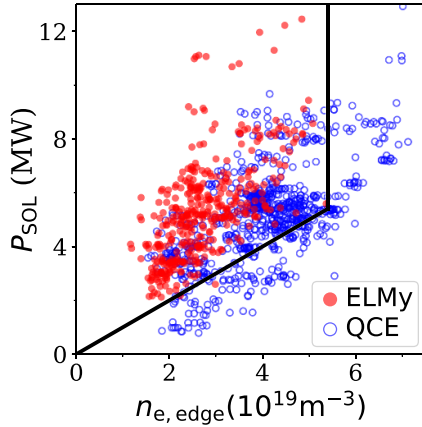
Figure 5. Power crossing the separatrix, P_{SOL} versus edge density $n_{e,edge}$. Open blue symbols represent QCE phases, filled red symbols represent type-I ELMy phases. The black line represents the boundary below which only data points in the QCE regime exist. It marks the area with $P_{SOL}(MW)/n_{e,edge}(10^{19}\,m^{-3}) < 1$ and/or $n_{e,edge} > 5.4 \cdot 10^{19}\,m^{-3}$.
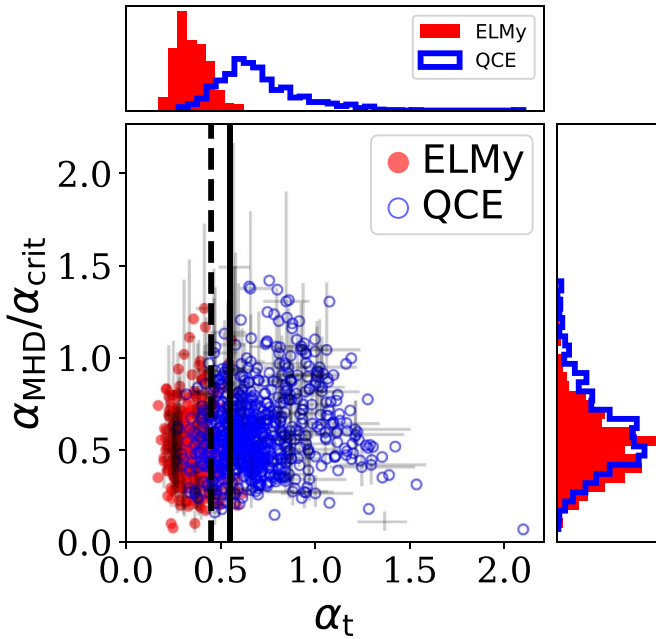
Figure 6. Normalised pressure gradient at the edge, $\alpha_{MHD}/\alpha_{crit}$, versus the turbulence control parameter α_t. Open blue symbols represent QCE phases, filled red symbols represent type-I ELMy phases. The black line at $\alpha_t = 0.45\,(0.55)$ represents the α_t values below (above) which nearly exclusively type-I ELM (QCE) data points exist. Representative error-bars are shown. The top (right) plot shows the histogram of α_t ($\alpha_{MHD}/\alpha_{crit}$).

$$\alpha_{MHD} = 4\mu_0 R_{geo} q_{cyl}^2 n_{e,edge} T_{e,edge} \langle \lambda_{p_e} \rangle^{-1} \qquad (8)$$

$$\alpha_{crit} = \kappa^{1.2} \cdot (1 + 1.5 \cdot \delta) \qquad (9)$$

with the poloidally averaged pressure fall-off length $\langle \lambda_{p_e} \rangle$. The normalised pressure gradient $\alpha_{MHD}/\alpha_{crit}$ corresponds to the closeness to the ideal ballooning limit with larger values

indicating that electromagnetic effects are becoming more important for the turbulence. The parameter α_t is linked to the α_d parameter of [33] and corresponds to transport by turbulence and is correlated with the strength of resistive ballooning modes [29].

It was shown in previous works that in QCE phases the pedestal foot, close to the separatrix but further inside than the analysis here, is ideal ballooning unstable in HELENA calculations [14, 15]. Here, however, both QCE as well as type-I ELMy phases exist for the full range of $\alpha_{MHD}/\alpha_{crit}$ covered in the data set. It is noted that a finite α_{MHD} is associated with H-mode conditions [20, 33, 34]. With the exception of a handful of outliers, all values in this data set are above $\alpha_{MHD}/\alpha_{crit} = 0.15$. This is consistent with the minimum values observed for type-I ELMy H-modes as presented in figure 1 of [19].

The α_t parameter sorts QCE and type-I ELMy phases remarkably well. Two boundaries are shown in figure 6 with vertical lines. For $\alpha_t < 0.45$ almost all data points show type-I ELMs while for $\alpha_t > 0.55$ almost all data points are in the QCE regime. In the range $0.45 < \alpha_t < 0.55$ we find signatures for both regimes. We note that the edge collisionality $\nu_{e,edge}^*$ sorts the data similarly well, with the boundary being $\nu_{e,edge}^* > 14$ for the absence of type-I ELMy data points. This can be seen in the absence of ELMy data points, $\max(E_{prox}) > 2$, above $\nu_{e,edge}^* > 14$ in figure 4.

Summarising the separatrix access conditions to QCE, we can state that engineering parameters are not sufficient, but both $\alpha_t > 0.55$ and $\nu_{e,edge}^* > 14$ provide a reliable description for the suppression of type-I ELMs.
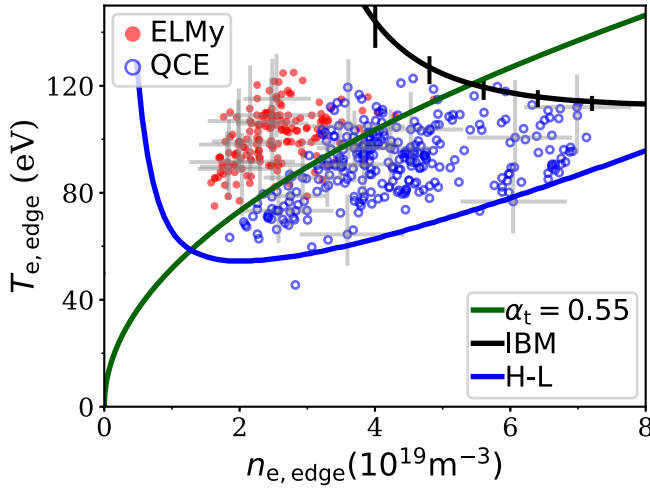
4. Separatrix operational space of QCE

The operational space in the *edge* (1 mm inside separatrix) parameters temperature $T_{e,edge}$ and density $n_{e,edge}$ is a concept to qualify the power exhaust capability of a regime as well as the limits in terms of ideal ballooning stability and nature of turbulence. Furthermore, also the operational window of the H-mode was shown to be well correlated with the separatrix parameters [20]. As indicated in figure 6 in the previous section, this concept could also be useful to distinguish between QCE and type-I ELMy phases.

The present data set covers the vast majority of the accessible H-mode separatrix operational space in ASDEX Upgrade. In this section the data set is limited to a fixed plasma current and toroidal magnetic field strength at which the majority of data points are taken. Table 2 presents the key parameters of this data set. The closeness to double-null is measured by the distance of the two X-points mapped to the outer mid-plane $d_{R,XP}$. This set is a sub-set of the set presented in section 2. Edge electron temperature and density measured by TS for this data set is shown in figure 7. The set consists of density (by fuelling with gas valves as well as pellets) and heating power variations, filling the high density part of the achievable H-mode space. The black and blue lines represent the ideal ballooning limit $\alpha_{MHD} = \alpha_{crit}$ and the H-L back transition criterion by Eich *et al* (equation (8) of [20]), respectively. The

Table 2. Main parameters of the data set used for the separatrix operational space with limited range in B_{tor} and I_p.

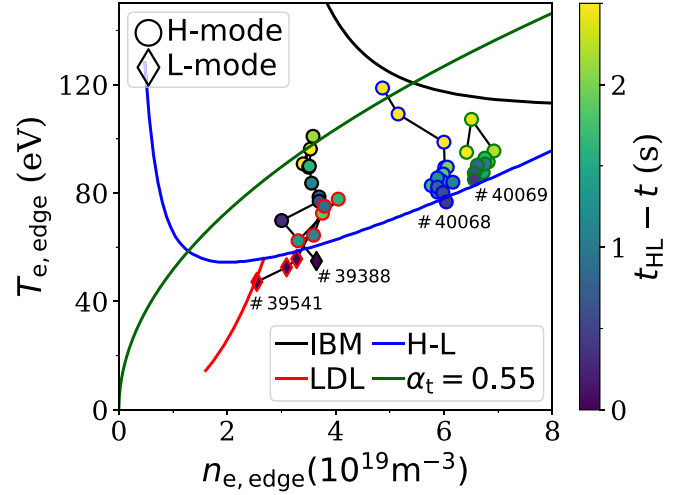| # points	# shots	B_{tor} (T)	I_p (MA)	q_{95}	κ	δ_{up}	$d_{R,XP}$ (mm)	P_{heat} (MW)	$n_{e,edge}$ (10^{19} m^{-3})
478	46	-2.47 ± 0.03	0.83 ± 0.01	5.5 ± 0.3	1.68 ± 0.04	0.2–0.4	6–25	1.2–15.8	1.6–7.1

Figure 7. Separatrix operational space in edge density $n_{e,edge}$ and temperature $T_{e,edge}$ of the data set with $B_{tor} = -2.5$ T and $I_p = 0.8$ MA. Open blue symbols represent QCE phases, filled red symbols represent type-I ELMy phases. The lines represent $\alpha_t = 0.55$ (green), H-L separation (blue) and ideal ballooning mode limit (IBM, black). Representative error-bars are shown. The error-bars for the black line represent the variation in α_{crit}.

Figure 8. Separatrix operational space in edge density $n_{e,edge}$ and temperature $T_{e,edge}$ for four discharges with $B_{tor} = -2.5$ T and $I_p = 0.8$ MA. These discharges exhibit an H-L back-transition due to a heating power ramp-down (# 39388 and # 39541) and fuelling ramp-up (# 40068 and # 40069). Color-coded is the time t relative to the H-L transition time t_{HL}. The circles represent data points in H-mode, diamonds represent data points in L-mode after the H-L transition. The lines represent the ideal ballooning mode limit (IBM, black), the L-mode density limit (LDL, red), $\alpha_t = 0.55$ (green) and the H-L separation (blue).

average $\alpha_{crit} = 2.88$ and equation (13), shown in section 5, is chosen to estimate the pressure fall-off length in order to infer the boundary lines. The error-bars for the black line represent the minimum and maximum of α_{crit} for the experimental data points close to the boundary. It is found that the data set reaches both boundaries. Figure 8 shows four discharges with an H-L back-transition. The transition is provoked by a heating power ramp-down and fuelling ramp-up (# 40068 and # 40069). For all four discharges the transition is close to the blue line, confirming the validity of this limit also at very high edge densities and for high plasma shaping.

In fact, this data set includes the highest edge density points in ASDEX Upgrade ever observed. The Greenwald density [35] for the discharge parameters is $n_{GW} = 1.0 \cdot 10^{20}$ m^{-3}, thus, the edge density spans a range of $n_{e,edge} = (0.2 - 0.7) n_{GW}$.

We reach here a higher value than the upper limit described in [36]. This can be explained by (i) a broadening of the pressure fall-off length compared to the scaling law taken in [36], leading to a lower α_{MHD} at similar edge electron density $n_{e,edge}$, and (ii) by the higher α_{crit} due to the higher plasma shaping. The ideal ballooning limit can be seen as a soft limit, rather leading to a broadening of the pressure fall-off length due to increased radial transport than an abrupt termination as expected in [36]. Indeed, the H-mode density limit was later

related with reaching the H-L back transition criterion shown as blue line in figure 7 as taken from [20].

An additional limit in the separatrix operational space is introduced here. In section 2 a criterion for the absence of type-I ELM was found using the turbulence control parameter α_t in line with the concept of the separatrix operational space. The green line in figure 7 represents $\alpha_t = 0.55$ which separates QCE and type-I ELMy phases. The QCE phases are between the green, black and blue lines and cover a substantial part of the operational space.

5. Pressure and power fall-off lengths

The loss of type-I ELMs is attributed to a change of turbulence near the separatrix as characterised by the turbulence control parameter α_t and an increase of the edge collisionality $\nu^*_{e,edge}$. The impact of this change on transport is studied in this section by looking at the fall-off lengths in the vicinity of the separatrix. Eich *et al* [19] found a broadening of the pressure fall-off length with increasing α_t for a data set excluding highly shaped plasma discharges; we apply the same analysis to our highly shaped plasma discharges.
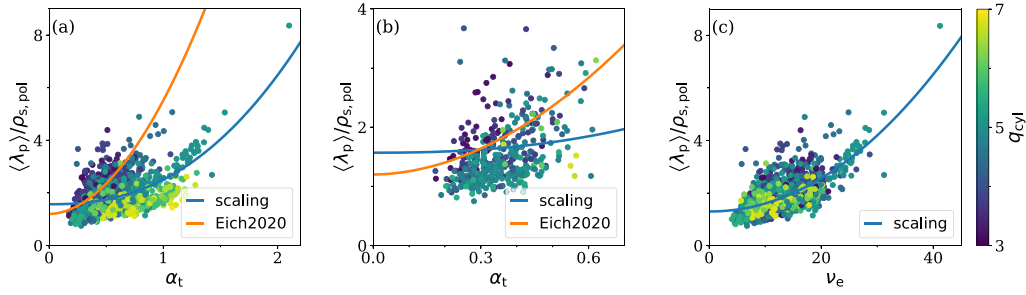
Figure 9. Poloidally averaged pressure fall-off length divided by the poloidal gyro-radius. Color-coded is the edge safety factor q_{cyl}. The plots (*a*) and (*b*) are as a function of α_t, (*c*) as a function of edge collisionality $\nu^*_{e,edge}$. (*b*) Zoom into (*a*) and only time points with type-I ELMs. The two lines in (*a*) and (*b*) represent the scaling law by Eich *et al* ([19], equation (11)) as well as a regression with the same function parameterisation for the presented data set equation (12). The line in (*c*) represents equation (13).

5.1. Electron pressure fall-off length in the vicinity of the separatrix

We discuss the electron pressure fall-off length just inside the separatrix ($-1\,\mathrm{mm} \pm 1.2 \cdot \langle\lambda_{p_e}\rangle$). In the work by Eich *et al* [19], the poloidally averaged pressure fall-off length $\langle\lambda_{p_e}\rangle$ was normalised to the poloidal gyro-radius

$$\rho_{s,pol} = \frac{\sqrt{m_D T_{e,sep}}}{e B_{pol}} \tag{10}$$

with m_D the deuterium ion mass. The regression result was

$$\langle\lambda_{p_e}\rangle / \rho_{s,pol} = 1.24 \cdot \left(1 + 3.6 \cdot \alpha_t^{1.9}\right). \tag{11}$$

The normalisation as well as the chosen function parameterisation ensure that at low values of α_t the well-known ITPA multimachine regression dependence [37] is obtained and the term including α_t resembles a broadening.

Here, we perform a regression analysis using the same function parameterisation for the present data set with the majority of points from highly shaped plasma discharges. We include all data points from section 2, notably with the full available range of plasma current and toroidal magnetic field and for both type-I ELMy and QCE regimes. Using the same functional as equation (11) we get

$$\langle\lambda_{p_e}\rangle / \rho_{s,pol} = 1.57 \cdot \left(1 + 0.60 \cdot \alpha_t^{2.39}\right) \tag{12}$$

with significantly less broadening in the available α_t range compared to equation (11). However, this regression has a low coefficient of determination $R^2 = 0.28$.

Figure 9(*a*) shows the data set as well as the two scaling laws using α_t. The data points in the type-I ELMy phases exhibit a large scatter with respect to α_t, but are equally represented with both regressions due to the limited range of α_t, see figure 9(*b*). However, it is observed that the scaling by Eich *et al*, equation (11), obtained from inter-ELM intervals in type-I ELMy phases, clearly overestimates the broadening with α_t in the present data set consisting of QCE phases at $\alpha_t > 0.55$. Moreover, a dependence on q_{cyl} remains, visible in the color-coding of figure 9(*a*).

We find a better representation of the data set using the edge collisionality

$$\langle\lambda_{p_e}\rangle / \rho_{s,pol} = 1.30 \cdot \left(1 + 0.002 \cdot \nu^{*2.0}_{e,edge}\right) \tag{13}$$

with an improved, but still low, $R^2 = 0.46$. The scaling with $\nu^*_{e,edge}$ with a linear q_{cyl} dependence captures the data better than the one with α_t with a quadratic q_{cyl} dependence, see figure 9(*c*).

5.2. Power fall-off length in the near scrape-off layer

A broadening of the power fall-off length in the QCE regime was first reported in [8]. Here, we expand the data set and analyse the dependence of the broadening on edge density $n_{e,edge}$, edge pressure $p_{e,edge}$ and turbulence control parameter α_t. We focus on time points in QCE, hence, without data from inter-type-I ELMs. A set of the data points is assembled, including 9 discharges in which IR data for the outer divertor target are recorded. All discharges are at $I_p = 0.8\,\mathrm{MA}$ and $B_{tor} = -2.5\,\mathrm{T}$.

The IR data analysis follows the routine analysis in ASDEX Upgrade [22]. Data is recorded in a sub-window mode allowing an increased frame rate of 1.5 kHz. Camera jitter is corrected and a line profile is extracted from the 2D data. Heat flux is calculated using the implicit implementation [38] of the THEODOR code [39]. A time average of 21 profiles is applied (14 ms) to average out the fast filamentary structures typically observed in the QCE regime [8, 16]. These profiles are fitted with the 1D diffusive model presented in [40]. To ensure reliable fitting result, a selection of data points is applied, keeping only values where the target value of power fall-off length λ_q is below 30 mm and where $\lambda_q > S$, with S being the divertor broadening. The measured λ_q is mapped to the outer mid-plane taking into account the poloidal flux expansion f_x for each time point, with $f_x \approx 5$ for the data set.

The power fall-off length λ_q as a function of edge electron density $n_{e,edge}$, separatrix electron pressure $p_{e,edge}$ and turbulence control parameter α_t is shown in figure 10. For the figure a further rolling average of 200 time points (133 ms) is applied. The corresponding standard deviation is around 15%. A strong correlation of λ_q with $n_{e,edge}$ and $p_{e,edge}$ is observed, while α_t yields no clear trend. The increase of λ_q with $n_{e,edge}$ and $p_{e,edge}$
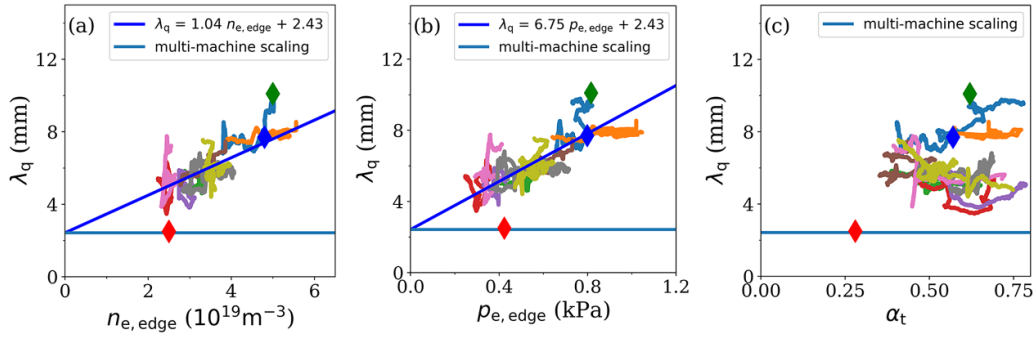
Figure 10. QCE power fall-off length mapped to the outer mid-plane λ_q as a function of (*a*) edge density $n_{e,edge}$, (*b*) edge pressure $p_{e,edge}$ and (*c*) turbulence control parameter α_t. The horizontal line represents the ITPA multi-machine scaling law, equation (14). The color-coding represents individual discharges. The diamonds represent three time points used in [8] with the red one being inter-type-I ELM and the blue and green ones in QCE.

is described as a linear trend starting with an offset corresponding to the ITPA multi-machine scaling law [37]

$$\lambda_q = 0.63 \cdot B_{pol,OMP}^{-1.19}. \tag{14}$$

The poloidal magnetic field at the outer mid-plane for this data set is $B_{pol,OMP} = 0.32$ T leading to the multi-machine scaling law prediction of $\lambda_q = 2.43$ mm. Note here, this data set is taken at a fixed plasma current and machine size, hence, no scaling with poloidal magnetic field B_{pol} is performed. Within this data set, no distinction between density and pressure dependence is possible due to the small variation in edge temperature.

In addition, three time points are shown that were used in [8] where the broadening of λ_q in QCE was investigated for the first time. It is observed that the time point marked with the red diamond is below the blue line. This time point is recorded in-between type-I ELMs. It is speculated that the enhanced filamentary transport of the QCE regime is leading to the broadening. A similar broadening of the scrape-off layer width with increasing density is found in a theory-based scaling law for L-mode conditions [41].

Future studies will be needed to reveal if other quantities such as current or machine size enter the broadening and to investigate the influence of plasma shaping. It was shown in TCV L-mode that high triangularity can be beneficial for a broad fall-off length [42]. The effect of B_{pol} could not be studied here and will need further attention as well as a multi-machine comparison to investigate potential major radius dependencies of the broadening.

6. Edge parameters and confinement

The access to the QCE regime is linked to a high turbulence control parameter and/or high edge collisionality, both achieved at high edge density. High edge density due to strong fuelling is correlated with a lower pedestal top pressure and a loss of confinement in type-I ELMy phases [43, 44]. This trend is also seen in the present data set. We investigate the consequences on confinement due to the operation in the QCE regime and the link to α_t.

Figure 11 shows the normalised energy confinement time H_{98y2} as a function of (a) edge density $n_{e,edge}$ and (b) turbulence control parameter α_t for the full data set of section 2, including all I_p and B_{tor} values. H_{98y2} decreases with both increasing $n_{e,edge}$ and α_t. QCE phases are at higher α_t compared to type-I ELMy phases and expose a reduced normalised energy confinement time. It has to be noted that at similar α_t no separation is observed and that close to the transition between type-I ELMs and QCE both regimes have $H_{98y2} = 0.8-1.0$. At very high α_t and high $n_{e,edge}$, the achievable normalised energy confinement time drops significantly, in line with previous observations in type-I ELMy H-mode [19].

In the following paragraph, we pay close attention to the vertical scatter in H_{98y2} of figure 11. For this, the data set is restricted to $B_{tor} = -2.5$ T and $I_p = 0.8$ MA as in section 4. Figure 12(*a*) presents the sub-set using color-coding for the total input power P_{tot}. It is observed that for a given α_t the highest normalised energy confinement time is achieved at lowest P_{tot}. Looking for the absolute value of the energy confinement time in figure 12(*b*), a strong P_{tot} dependence is observed. Thus, the power degradation in this data set is stronger than predicted by the scaling law.

In order to investigate whether the change in confinement stems from the core or the pedestal region, the pedestal top pressure is now investigated. Looking into the pedestal top pressure instead of the normalised energy confinement time reveals a similar trend. Figure 13 shows the pressure at the pedestal top, taken at $\rho_{pol} = 0.9$, as a function of the turbulence control parameter α_t for the data set with $B_{tor} = -2.5$ T and $I_p = 0.8$ MA and for QCE phases only. The highest pedestal top pressure is achieved at lowest α_t. Both, increasing $n_{e,edge}$ or decreasing $T_{e,edge}$ increases α_t and lowers the pedestal top pressure. In addition, at constant α_t a higher pedestal top pressure is achieved at higher heating power. HELENA calculations show that both pedestal top and foot are close to the ideal ballooning limit in QCE. High pedestal top pressure is achieved when the steep gradient region in-between is in the 2nd stability region [14].

As a conclusion, a high α_t value is penalised by a reduced normalised energy confinement time. As the pedestal top pressure shows a similar trend, we conclude that the change in confinement is mainly pedestal driven. It is shown that QCE and
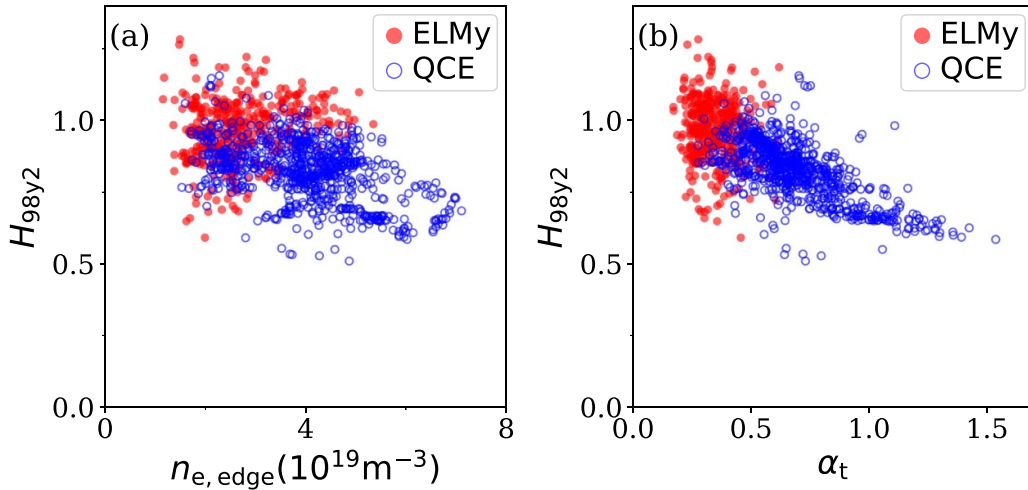
Figure 11. Normalised energy confinement time H_{98y2} as a function of (*a*) edge density $n_{e,edge}$ and (*b*) turbulence control parameter α_t. Open blue symbols represent QCE phases, filled red symbols represent type-I ELMy phases.
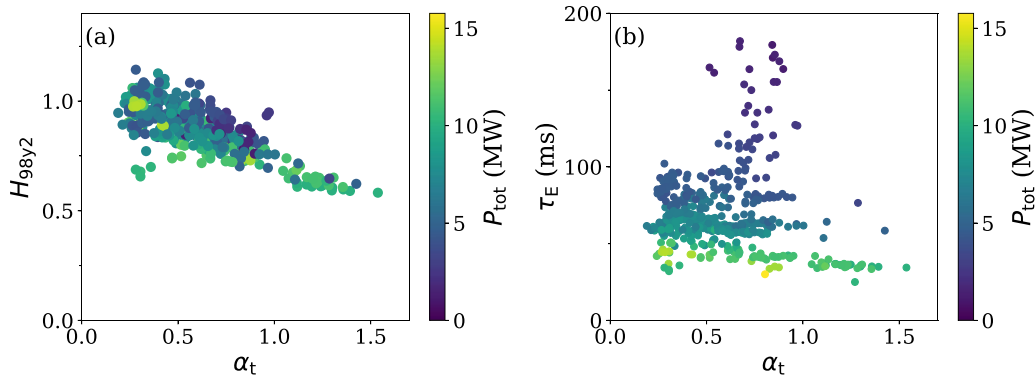
Figure 12. (*a*) Normalised energy confinement time H_{98y2} as a function of the turbulence control parameter α_t for the data set with $B_{tor} = -2.5\,\text{T}$ and $I_p = 0.8\,\text{MA}$ for both type-I ELMy and QCE phases. (*b*) The same for the energy confinement time. Color-coded is the total input power P_{tot}.
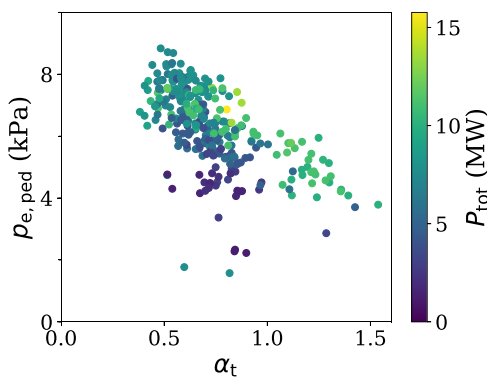
Figure 13. Pedestal top pressure $p_{e,ped}$ as a function of the turbulence control parameter α_t for the data set with $B_{tor} = -2.5\,\text{T}$ and $I_p = 0.8\,\text{MA}$ for QCE phases. Color-coded is the total input power P_{tot}.

type-I ELM phases have the same connection between edge parameters and energy confinement. The QCE phases with the highest normalised energy confinement time are close to the boundary to type-I ELMs.

7. Scenario performance

In the previous sections, it was shown that the QCE regime occurs at high edge density and large values of the turbulence control parameter α_t. Its advantageous aspects, the suppression of type-I ELMs and a longer power fall-off length, are bought with a moderate confinement loss. In this section, the QCE scenario is further developed in terms of its reactor relevance.

7.1. Route towards low edge safety factor

Low edge safety factor q_{95} operation is expected for a viable reactor solution with high fusion gain. In a future reactor-sized tokamak, low $q_{95} \approx 3$–4 is envisaged [45]. Contrary to that, it was shown that the QCE regime is more readily available at elevated q_{95}. This can be explained by higher q_{95} increasing α_t and $\nu^*_{e,edge}$. Hence, less pressure or density at the plasma boundary is needed to reach the necessary access conditions.

The edge safety factor range of the QCE regime in ASDEX Upgrade was successfully lowered to $q_{95} \approx 3.3$. Figure 14
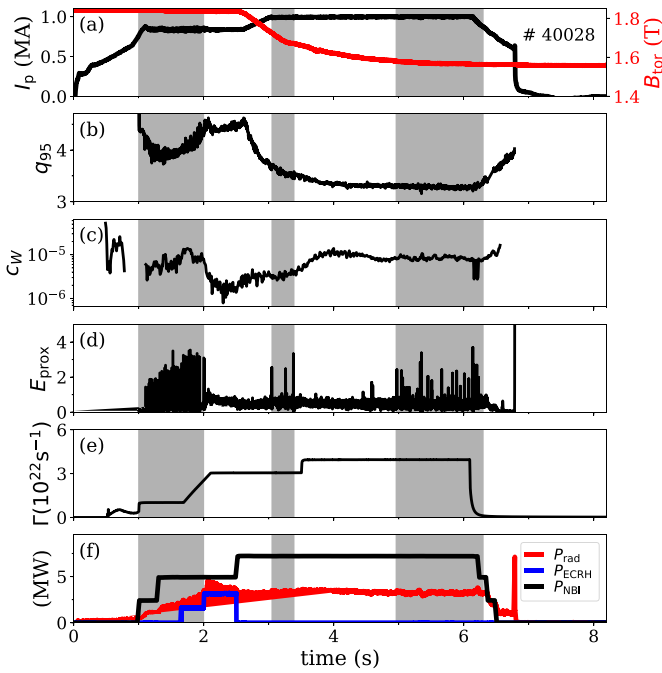
Figure 14. Time traces of ASDEX Upgrade discharge #40028. (*a*) Plasma current I_p (black) and toroidal magnetic field B_{tor} (red) are ramped up and down, respectively. This reduces the edge safety factor q_{95} as displayed in (*b*). Core tungsten concentration c_W is shown in (*c*). In (*d*) the ELM proxy E_{prox} is shown. The QCE is interrupted during the I_p ramp when type-I ELMs re-appear. The QCE regime goes back to a type-I ELMy H-mode at 5 s. In (*e*) the deuterium gas flux Γ is shown. Heating and radiated power is shown in (*f*). X3 ECRH is applied during the H-mode entry and plasma shaping ramp until 2.5 s before B_{tor} is ramped down. Phases with type-I ELMs are marked in grey.

shows time traces of the final discharge of a series of four consecutive discharges with step-wise lowering the toroidal magnetic field and increasing the plasma current while adjusting the fuelling level. The plasma start-up into the final shape is performed at $B_{tor} = -1.8\,T$ with central wave heating until the ELM-free QCE phase is fully established. In order to lower the safety factor the toroidal magnetic field is ramped during the discharge towards $B_{tor} = -1.5\,T$ starting at 2.5 s (figure 14(*a*)). The final value is slowly approached at 5.5 s due to the large inductance of the coils. At these levels no central wave heating is available in ASDEX Upgrade. After 2.5 s the central X3 ECRH is switched off and compensated by increasing the neutral beam power, shown in figure 14(*f*). The tungsten concentration in the core is counteracted by MHD activity appearing at 4.0 s in this discharge. The plasma current is increased from 0.8 MA to 0.94 MA at 3.0 s (figure 14(*a*)). With higher plasma current, more fuelling is applied to prevent type-I ELMs from emerging as shown for previous QCE studies [6]. This is also seen by the re-appearance of irregular type-I ELMs after 5.0 s showing that the chosen fuelling amount is marginal for the given safety factor. The type-I ELMs re-appear later in the presented discharge compared to the preceding discharge with lower fuelling level. With additionally increased fuelling level the onset of type-I ELMs might be further delayed or suppressed. An increased plasma shaping might also improve the

access window of QCE. The time point of the type-I ELM re-appearance coincides with $q_{95} \approx 3.3$ and marks the end of the QCE phase.

7.2. Low tungsten core concentration

The QCE scenario provides good intrinsic impurity control in all of the exploited operational range. Figure 15 shows the core tungsten concentration c_W for the data set of section 4 with $B_{tor} = -2.5\,T$ and $I_p = 0.8\,MA$. Central wave heating is used for the majority of data points, which is typically applied for ASDEX Upgrade tungsten operation [46]. The core tungsten concentration correlates with both the ELM proxy $\max(E_{prox})$ and the turbulence control parameter α_t. A reduced level of core tungsten is observed in QCE compared to type-I ELMy H-mode. This correlates with the reduction of the impurity source due to the absence of sputtering during type-I ELMs.

A correlation of lower tungsten concentration with increasing α_t is observed. It is speculated that the particle and impurity outward transport at the edge of the plasma is increased by the local ballooning modes. The two branches visible for the QCE regime are due to a change in $T_{e,sep}$. A lower tungsten concentration is observed at lower $T_{e,sep}$ values in phases with lower heating power.

8. Avoiding large ELMs from start to end of a discharge

While in ITER transient phases with type-I ELMs—at reduced plasma current or mitigated through reduced pedestal top pressure—might be acceptable regarding divertor power load [47], DEMO studies often focus on regimes without any type-I ELMs [45]. We investigate in this section the feasibility of entering the QCE regime without any transient type-I ELM phase. Furthermore, in the previous sections only plasma discharges without seeding are discussed. Here, we show that QCE discharges can transit into a nitrogen seeded, partially detached steady state phase at high normalised energy confinement time.

8.1. Overview of the discharge

We focus on ASDEX Upgrade discharge #37164. For the first time a double feed-back controlled discharge was achieved by using neutral beam injection to control β_{pol} and nitrogen seeding to control the divertor electron temperature T_{div}.

Figure 16 shows time traces of the most important parameters of this discharge. Panel (*a*) shows the plasma current and stored energy. The plasma current is ramped up from $I_p = 0.6\,MA$ to $I_p = 1.0\,MA$ in the QCE phase, resulting in $q_{95} = 4.6$ in the flat-top. The discharge starts at low current and the density is increased already in L-mode to very high levels. H-mode is entered at these high densities and low currents, so that already the initial H-mode phase is a phase without ELMs. Subsequently, both current and heating power are simultaneously increased together with the gas puff. This is a delicate path through the operational space, as only slight misalignments lead to the occurrence of ELMs. Our way to
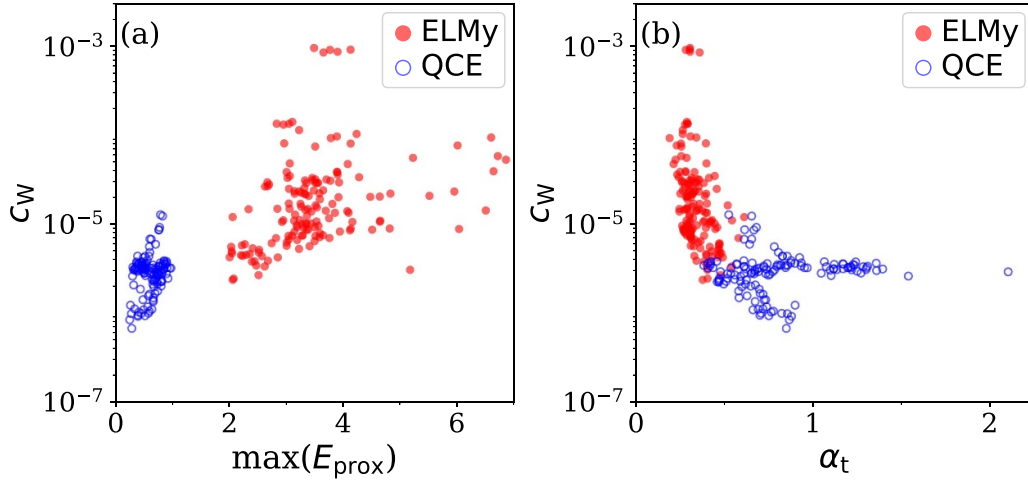
Figure 15. Core tungsten concentration c_w as a function of (*a*) the ELM proxy $\max(E_{prox})$ and (*b*) the turbulence control parameter α_t. QCE phases ($E_{prox} < 1$) exhibit low core tungsten concentrations.
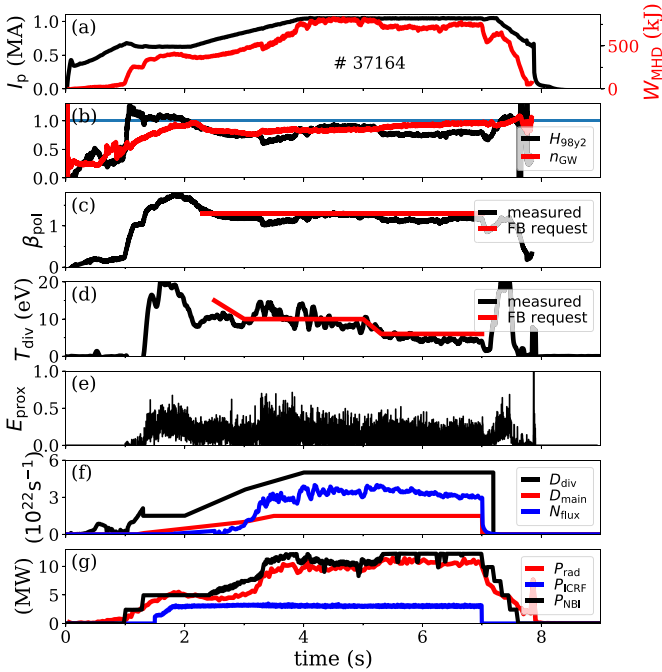
Figure 16. Time traces of ASDEX Upgrade # 37164. (*a*) Plasma current I_p (black) and stored energy W_{MHD} (red). (*b*) Normalised energy confinement time (H_{98y2}, black) and density (Greenwald density fraction n_{GW}, red). (*c*) Normalised poloidal plasma pressure β_{pol}, measured (black) and feed-back request (red). (*d*) Divertor temperature estimate from shunt current T_{div}, measured (black) and feed-back request (red). (*e*) ELM proxy E_{prox} derived from the divertor shunt currents. (*f*) Fuelling levels, deuterium fuelling is provided by gas valves in the divertor D_{div} and main chamber D_{main}. The nitrogen flux N_{flux} from the divertor is feed-back controlled by T_{div}. (*g*) Heating and radiated power levels, a constant ICRF power P_{ICRF} is applied together with the feed-back controlled neutral beam power P_{NBI}. The radiated power P_{rad} is estimated from bolometric reconstruction.

achieve this successful discharge was to program the gas fuelling feed forward and additionally employ dual feedback: on β_{pol} to control the heating power and on T_{div} to keep the edge

cool and the edge collisionality high. The β_{pol} (*c*) and T_{div} (*d*) controllers are active from 2.3 s and 2.5 s, respectively. A constant $\beta_{pol} = 1.3$ is requested. The T_{div} request value is slowly lowered from 15 eV at 2.5 s to 10 eV at 3.0 s. This allows to avoid large variations in the nitrogen flux which can lead to controller oscillations. Two flat-top values are programmed, $T_{div} = 10$ eV (3.0–5 s) and later $T_{div} = 6$ eV (5.3–7.0 s). Deuterium is puffed both from the divertor volume as well as main chamber positions in a feed-forward waveform, increasing during the I_p ramp as shown in panel (*f*). The feed-back controlled nitrogen gas puff increases sharply at the start of the $T_{div} = 10$ eV request. The requested nitrogen seeding rate then reaches a near constant level with a slow decline, a typical behaviour due to the increased amount of nitrogen stored in the wall throughout a discharge [48].

As shown in panel (*c*), the maximum neutral beam heating power of $P_{NBI} = 12.0$ MW that was set for the controller is not sufficient to keep $\beta_{pol} = 1.3$ when approaching $T_{div} = 6$ eV. With the additional seeding the line averaged electron density approaches the Greenwald density and a reduction of the energy confinement time is observed, leading also to a drop of the normalised energy confinement time from $H_{98y2} = 0.9$ to 0.75, shown in panel (*b*). The drop of β_{pol} at constant heating power is reflected in the reduction of W_{MHD}.

8.2. Initial discharge phase and H-mode entry

Figure 17 shows time traces of the initial L-mode phase and the entry into H-mode. Panels (*a*) and (*b*) show the evolution of the stored energy and the density, respectively. In the grey area of panel (*b*) the density signal is perturbed by a MARFE [49], propagating up- and downwards on the high field side. This indicates that the fuelling and the separatrix density are very close to the maximum achievable value before leading to an L-mode density limit in ASDEX Upgrade [50, 51]. The necessary fuelling level to stay away from the disruptive density limit depends on the machine conditions. The appearance of the MARFE is not needed for the transition to the QCE phase and should be avoided. In the
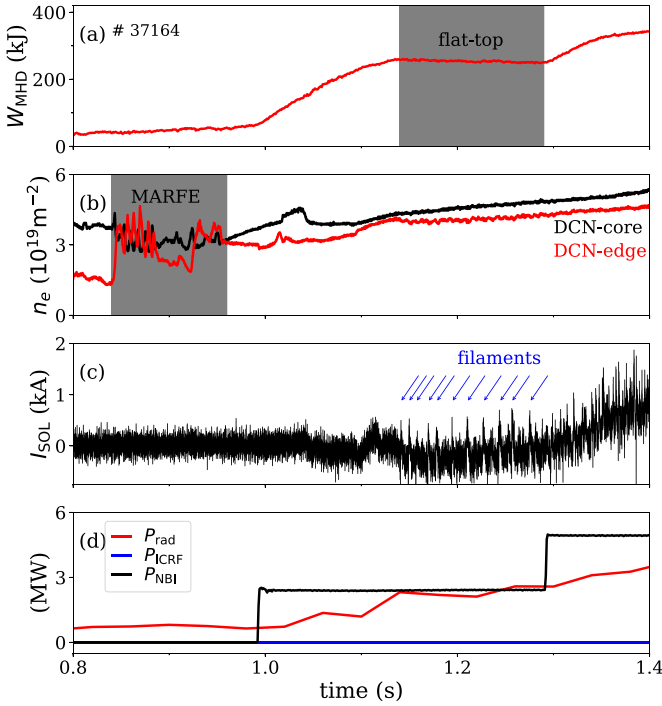
Figure 17. Time traces of the H-mode entry of the discharge from figure 16. (*a*) Stored energy W_{MHD}. (*b*) Line integrated density of the DCN laser interferometer in the core (DCN-core) and edge (DCN-edge). (*c*) Divertor shunt current at the outer target I_{pol} used to mark time points with transient fluxes towards the divertor. (*d*) Heating and radiated power levels. Two steps of neutral beam power P_{NBI} are applied to transition into H-mode, ICRF power P_{ICRF} is increased after the shown time window. The radiated power P_{rad} is inferred from a bolometric reconstruction. It increases in line with the density increase.

future, a feed-back controlled fuelling trajectory in this phase is envisaged, similar to the H-mode density limit avoidance of [51].

The H-mode is achieved with the first step in neutral beam power. In this phase, the plasma current is low and $q_{95} = 7.8$. The high q_{95} allows an easier access to the type-I ELM free QCE regime [1, 6]. After the L-H transition the stored energy increases, reaching a flat-top when low-amplitude filaments appear. The transition to the close to double-null shape is initiated after the L-H transition. A ramp-up in plasma current is done after achieving the close to double-null shape.

8.3. Influence of nitrogen seeding on divertor conditions

Figure 18 shows Langmuir probe (LP) measurements from the outer divertor target in order to study the divertor state and the influence of the enhanced pedestal foot transport onto the divertor conditions. The grey dots represent single LP measurement time points, whereas the blue and red lines correspond to the lower envelope (0.05 quantile) to represent the value in-between filaments and an average (median, 0.5 quantile) over 30 ms, respectively. It is shown that the introduction of nitrogen leads to a partially detached outer divertor. A strong reduction of particle flux and electron temperature in-between filaments is observed. It is found that the filaments lead to an

increase in particle flux and are dominating the overall particle flux to the target after nitrogen is introduced.

In the following paragraphs we discuss the evolution in detail. Figure 18(*a*) shows the integrated ion saturation current $J_{tot} = 2\pi R \int j_{sat}\, ds$ along the outer divertor target coordinate s. Both curves show a clear reduction by ramping up the nitrogen puff level at 3.0 s. The lower envelope (blue line) decreases significantly, $J_{tot} = 20$ kA to 5 kA. The median value (red) decreases only moderately, $J_{tot} = 25$ kA to 19 kA. While J_{tot} in-between filaments reaches very low levels, the average value slowly decays towards a final value, $J_{tot} \approx 10$ kA.

Figure 18(*b*) shows the peak electron temperature along the outer divertor target probes $T_{e,tgt}$ together with the T_{div} feed-back request trajectory in black. The control in such QCE discharges in ASDEX Upgrade works successfully, as the time-averaged peak temperature from the LPs and the T_{div} request agree reasonably. The time-averaged peak electron temperature at the outer divertor falls below 10 eV, however, single filaments clearly exceed this value. The peak temperature in-between filaments (blue line) drops with the start of nitrogen seeding to $T_{e,tgt} \leqslant 5$ eV. The temperature during filaments is likely over-estimated. The estimation of $T_{e,tgt}$ using triple probes assumes equal plasma parameters at all three probe locations which is potentially not given. Figure 18(*c*) shows the floating potential of one LP at $\rho_{pol} = 1.03$. The floating potential is linked to the electron temperature but measured at a single location, thus, capable of resolving spatially small structures. It reaches about zero after 3.0 s and the filaments do not lead to a significant excursion.

It is conclude that the divertor is in a detached state in-between filaments and on average partial detachment is reached. However, single filaments still lead to a high ion saturation current, while the divertor temperature is ambiguous and needs further analysis.

9. Discussion

9.1. Projection to ITER-like plasma parameters

In this section a projection to ITER-like parameters is performed. Limits for the achievable separatrix density, turbulence control parameter α_t and collisionality $\nu^*_{e,edge}$ are derived using estimates of the separatrix conditions and varying assumptions of the fall-off lengths. These values are then compared to the conditions in which at ASDEX Upgrade the QCE regime is found.

We take ITER parameters, major radius of $R_{geo} = 6.2$ m, minor radius of $a_{geo} = 2.0$ m, elongation of $\kappa = 1.8$, averaged triangularity of $\delta = 0.49$, toroidal magnetic field of $B_{tor} = 5.3$ T, plasma current of $I_p = 15$ MA and edge safety factor of $q_{cyl} = 3.0$. Additionally, it is assumed that the power crossing the separatrix is $P_{SOL} = 100$ MW and $Z_{eff} = 1.5$–2.5 at the separatrix [52]. For the power fall-off length three values are taken. The smallest value of $\lambda_q = 0.9$ mm corresponds to the extrapolation by Eich *et al* [40]. The largest value of $\lambda_q = 3.6$ mm corresponds to the value chosen for the SOL/divertor simulations for ITER by Kukushkin *et al* [11]. Recent gyrokinetic simulations predict an even larger value [53]. A
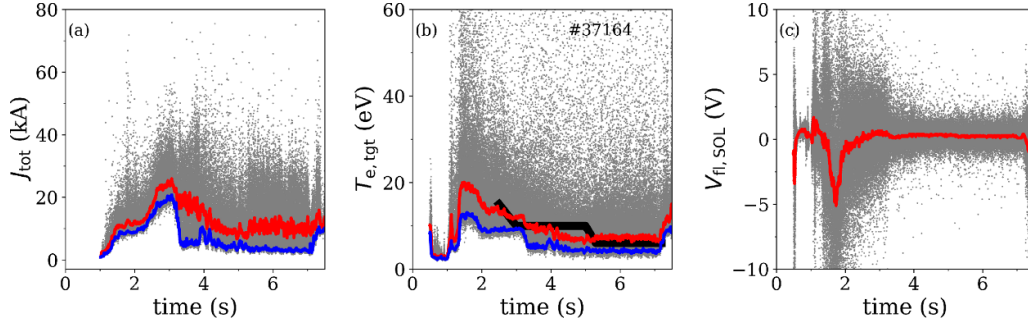
Figure 18. Local quantities at the outer divertor target measured by Langmuir probes; (*a*) integrated ion saturation current, (*b*) maximum electron temperature and (*c*) floating potential of a single probe in the scrape-off layer at $\rho_{pol} = 1.03$. The blue and red lines correspond to the lower envelope (0.05 quantile) and median (0.5 quantile) over 30 ms, respectively. The black line in (*b*) corresponds to the T_{div} feedback request.

Table 3. Scan of λ_q with fixed $Z_{eff} = 2.0$.

λ_q (mm)	$T_{e,edge}$ (eV)	$n_{e,edge}^{IBM}$ (10^{19} m^{-3})	$n_{e,edge}^{IBM}$ / n_{GW}	α_t^{IBM}	$\nu_{e,edge}^{*,IBM}$
0.9	295	3.3	0.28	0.13	4
1.8	221	7.5	0.63	0.55	18
3.6	174	17.8	1.50	2.12	70

Table 4. Scan of Z_{eff} with fixed $\lambda_q = 1.8$ mm.

Z_{eff}	$T_{e,edge}$ (eV)	$n_{e,edge}^{IBM}$ (10^{19} m^{-3})	$n_{e,edge}^{IBM}$ / n_{GW}	α_t^{IBM}	$\nu_{e,edge}^{*,IBM}$
1.5	214	7.8	0.66	0.46	15
2.0	221	7.5	0.63	0.55	18
2.5	228	7.3	0.61	0.63	21

medium value of $\lambda_q = 1.8$ mm is added. Temperature, density and pressure fall-off length are estimated self-consistently with the chosen power fall-off length by using $\lambda_{n_e}/\lambda_{T_e} = 3/2$. Furthermore, assuming Spitzer–Härm electron heat conduction being the dominant heat transport channel gives $\lambda_{T_e}/\lambda_q = 7/2$ and $\lambda_{p_e}/\lambda_q = 21/10$. These relations are shown to be consistent with measurements in ASDEX Upgrade [25, 26, 36, 54] and JET [36, 55]. Note, poloidally averaged values are a factor 16/9 larger than the values at the outer mid-plane [40].

We use Spitzer-Härm electron heat conduction to estimate the separatrix temperature, equation (5). For the given gradient and estimated temperature, we calculate the density $n_{e,edge}^{IBM}$ for which the ideal ballooning mode limit (IBM, $\alpha_{MHD} = \alpha_{crit}$, see equations (8) and (9)), is reached. With this density, we calculate the turbulence control parameter α_t^{IBM}, equation (7), and the edge collisionality $\nu_{e,edge}^{*,IBM}$, equation (6). The choice of focusing on the ideal ballooning mode limit is because it allows a self-consistency check of fall-off length with $n_{e,edge}^{IBM}$, α_t^{IBM} and $\nu_{e,edge}^{*,IBM}$. HELENA calculations confirm that an ITER-like pedestal with steep gradients is likely ballooning unstable at the pedestal foot supporting the existence of QCE at ITER-like parameters [14]. Further limitations outside the scope of this analysis are posed by avoiding H-L back transitions as well as excessive degradation of the pedestal pressure.

Table 3 shows the calculated values for the three power fall-off lengths taking $Z_{eff} = 2.0$. For the smallest value of $\lambda_q = 0.9$ mm, the maximum $n_{e,edge}$ given by the ideal ballooning limit is very low, leading together with the high $T_{e,edge}$ to an $\alpha_t^{IBM} = 0.13$ and $\nu_{e,edge}^{*} = 4$. At this value of α_t and/or $\nu_{e,edge}^{*}$ a type-I ELMy H-mode is always observed in ASDEX Upgrade. The situation gets more relaxed with a broader λ_q through the increased achievable $n_{e,edge}$, α_t and $\nu_{e,edge}^{*}$. With $\lambda_q = 1.8$ mm

a larger $\alpha_t^{IBM} = 0.55$ and $\nu_{e,edge}^{*,IBM} = 18$ is calculated. This value of α_t and/or $\nu_{e,edge}^{*}$ is sufficient to obtain QCE for the ASDEX Upgrade data set. For the largest value, $\lambda_q = 3.6$ mm, the ideal ballooning limit for $n_{e,edge}$ is above the Greenwald limit $n_{e,edge}^{IBM}$ / $n_{GW} = 1.5$. This is interpreted that the actual limit is not set by ideal ballooning modes but rather by other effects. Not reaching the ideal ballooning limit but still having $\alpha_t > 0.55$ and/or $\nu_{e,edge}^{*} > 14$ shows in ASDEX Upgrade the access to QCE but not reaching the highest pedestal top pressures.

So far we chose a fixed $Z_{eff} = 2.0$. A variation in Z_{eff} will lead to a modest change in the parameters. Taking the middle value of λ_q, the influence of Z_{eff} is presented in table 4. A variation from $Z_{eff} = 1.5$–2.5 does not change the conclusions of the previous paragraph. A lower $Z_{eff} = 1.5$ leads to a 4% higher $n_{e,edge}^{IBM}$ and a 16% lower α_t^{IBM} and $\nu_{e,edge}^{*,IBM}$. A higher $Z_{eff} = 2.5$ leads to a 3% lower $n_{e,edge}^{IBM}$ and a 15% higher α_t^{IBM} and $\nu_{e,edge}^{*,IBM}$.

As a conclusion, very small values of λ_q are only self-consistent with a low edge density due to the ideal ballooning mode limit. Reaching QCE with ITER-like plasma parameters seems plausible with a λ_q broader than the empirical extrapolation by Eich *et al* [40] and at elevated edge densities. Indeed, a broadening is observed when increasing the density in the presented study in ASDEX Upgrade.

9.2. Access to detachment and seeding

We have shown that nitrogen seeding is compatible with the QCE regime in ASDEX Upgrade. However, in this initial experiments filaments are not buffered, e.g. still leading to an increased particle flux to the divertor target. This is a potential obstacle for the QCE regime as reactor-relevant alternative. Experiments as well as modelling will be needed to investigate if the filamentary heat and particle flux can be buffered along

the open field lines in the scrape-off layer and—if buffering is possible—how to control the dynamic radiation/detachment state in the divertor.

The QCE filaments are thought to originate close to the separatrix. Thus, the ion temperature is of the order of the separatrix temperature. Low amplitude type-III ELMs were successfully buffered in JET [13] demonstrating that ions with such energies interact with the divertor plasma and are able to dissipate part of their energy. Future research has to address the particle flux due to the QCE filaments and verify if they can be buffered sufficiently to achieve low material erosion.

Furthermore, the increased cross-field transport in QCE leads to a density shoulder in ASDEX Upgrade. It was shown that the first wall loading increases with increasing α_t [56]. Future studies have to assess if the first wall loading and the associated sputtering is acceptable for a reactor-sized tokamak.

10. Summary and conclusions

In the present contribution, the operational limits of the QCE regime are analysed and expanded. The transition from type-I ELMs to QCE is gradual. The definition of an automatic ELM proxy using the shunt currents measured at the divertor target allows to distinguish phases with type-I ELMs from QCE phases. The absence of type-I ELMs is correlated with high values of the edge collisionality of $\nu_{e,edge}^* > 14$ and of the turbulence control parameter of $\alpha_t > 0.55$, where edge refers to the area 1 mm inside the separatrix.

The concept of a separatrix operational space was presented in [20], showing that H-mode conditions have different boundaries to L-mode, density limit and ideal ballooning limit. These boundaries are shown to also apply towards very high density for discharges in the QCE regime with high plasma shaping. An additional boundary is added for the transition from type-I ELMs to QCE by $\alpha_t > 0.55$.

The loss of type-I ELMs is attributed to a change of turbulence near the separatrix as characterised by α_t and/or $\nu_{e,edge}^*$. The impact of this change on transport was also studied. The pressure fall-off length at the pedestal foot measured by Thomson scattering is smaller than that predicted by the inter-ELM H-mode scaling of [19]. A regression analysis reveals that the broadening is better described by the linear q_{cyl} dependence of $\nu_{e,edge}^*$ instead of the quadratic dependence of α_t. The power fall-off length measured by infrared thermography is significantly wider in QCE compared to the ITPA multi-machine, inter-ELM scaling [8]. For the available data set, at fixed I_p and B_{tor}, the increase is best described by a linear correlation with $n_{e,edge}$ and $p_{e,edge}$. Other dependencies need to be shown in the future, e.g. by multi-machine approaches.

The near separatrix parameters also affect core confinement. The normalised energy confinement time decreases with increasing $n_{e,edge}$ and α_t in the presented data set, consistent with previous works in type-I ELMy H-mode [43, 44]. QCE and type-I ELMy phases at similar α_t exhibit similar H_{98y2}

values. At the highest pedestal top pressure the edge is close to the ideal ballooning mode limit, consistent with previous HELENA calculations [14].

The boundary parameters not only influence the plasma core, but also determine the interaction with the wall and the source of impurities. In QCE the tungsten concentration in the core plasma is lower than in type-I ELMy phases, correlated with the increased α_t.

Two major steps for the reactor-relevance of the scenario are achieved. First, the QCE regime is successfully demonstrated for a low edge safety factor of $q_{95} = 3.3$. Second, the access to QCE is possible in a demonstration discharge (i) without transient phase with large type-I ELMs, (ii) with a transition to a partially detached divertor and (iii) with high normalised confinement. This is achieved by a double feed-back on β_{pol} and T_{div} used for the first time in ASDEX Upgrade.

We propose a potential route to a safe start-up of a large scale tokamak: we showed that the operational space in terms of separatrix density is significantly larger than previously anticipated, e.g. in [36]. Hence, it is possible to start with very high separatrix density and sacrificing partially confinement. After learning to operate the machine in a safe way one then can reduce the separatrix density close to the border between QCE and type-I ELMy phases within a power exhaust solution to recover the necessary confinement but still operate without large scale transients. It is hence not critical to extrapolate the exact point between type-I ELMy phase and QCE for a larger machine but it is very critical to confirm the large operational density window also in larger machines.

ORCID iDs

M. Faitsch ● https://orcid.org/0000-0002-9809-7490
T. Eich ● https://orcid.org/0000-0003-3065-8420
G.F. Harrer ● https://orcid.org/0000-0002-1150-3987
E. Wolfrum ● https://orcid.org/0000-0002-6645-6882
D. Brida ● https://orcid.org/0000-0002-8647-7058
P. David ● https://orcid.org/0000-0003-4837-8507
M. Dunne ● https://orcid.org/0000-0002-5259-9970
L. Gil ● https://orcid.org/0000-0002-9970-2154
B. Labit ● https://orcid.org/0000-0002-0751-8182
U. Stroth ● https://orcid.org/0000-0003-1104-2233

References

[1] Stober J., Maraschek M., Conway G.D., Gruber O., Herrmann A., Sips A.C.C., Treutterer W. and Zohm H. (The ASDEX Upgrade Team) 2001 *Nucl. Fusion* **41** 1123

[2] Saibene G. *et al* 2005 *Nucl. Fusion* **45** 297

[3] Perez von Thun C.P. *et al* 2008 *Plasma Phys. Control. Fusion* **50** 065018

[4] Wolfrum E. *et al* 2011 *Plasma Phys. Control. Fusion* **53** 085026

[5] Kirk A., Muller H.W., Wolfrum E., Meyer H., Herrmann A., Lunt T., Rohde V. and Tamain P. 2011 *Plasma Phys. Control. Fusion* **53** 095008

[6] Harrer G. *et al* 2018 *Nucl. Fusion* **58** 112001

[7] Labit B. *et al* 2019 *Nucl. Fusion* **59** 086020

[8] Faitsch M., Eich T., Harrer G.F., Wolfrum E., Brida D., David P., Griener M. and Stroth U. 2021 *Nucl. Mater. Energy* **26** 100890

[9] Greenwald M. *et al* 1999 *Phys. Plasmas* **6** 1943

[10] Gil L. *et al* 2020 *Nucl. Fusion* **60** 054003

[11] Kukushkin A., Pacher H.D., Pacher G.W., Kotov V., Pitts R.A. and Reiter D. 2013 *J. Nucl. Mater.* **438** S203

[12] Goldston R., Reinke M.L. and Schwartz J.A. 2017 *Plasma Phys. Control. Fusion* **59** 055015

[13] Rapp J., Eich T., Hellermann M.V., Herrmann A., Ingesson L.C., Jachmich S., Matthews G.F., Philipps V. and Saibene G. (Contributors to the EFDA-JET Workprogramme) 2002 *Plasma Phys. Control. Fusion* **44** 639

[14] Radovanovic L., Dunne M., Wolfrum E., Harrer G., Faitsch M., Fischer R. and Aumayr F. 2022 *Nucl. Fusion* **62** 086004

[15] Harrer G.F. *et al* 2022 *Phys. Rev. Lett.* **129** 165001

[16] Griener M. *et al* 2020 *Nucl. Mater. Energy* **25** 100854

[17] Carralero D., Birkenmeier G., Müller H.W., Manz P., deMarne P., Müller S.H., Reimold F., Stroth U., Wischmeier M. and Wolfrum E. 2014 *Nucl. Fusion* **54** 123005

[18] Giacomin M., Pau A., Ricci P., Sauter O. and Eich T. (The ASDEX Upgrade Team, JET Contributors and The TCV team) 2022 *Phys. Rev. Lett.* **128** 185003

[19] Eich T., Manz P., Goldston R.J., Hennequin P., David P., Faitsch M., Kurzan B., Sieglin B. and Wolfrum E. 2020 *Nucl. Fusion* **60** 056016

[20] Eich T. and Manz P. (The ASDEX Upgrade Team) 2021 *Nucl. Fusion* **61** 086017

[21] Kallenbach A., Carlson A., Pautasso G., Peeters A., Seidel U. and Zehrfeld H.-P. 2001 *J. Nucl. Mater.* **290–293** 639

[22] Sieglin B., Faitsch M., Herrmann A., Brucker B., Eich T., Kammerloher L. and Martinov S. 2015 *Rev. Sci. Instrum.* **86** 113502

[23] Kurzan B. and Murmann H.D. 2011 *Rev. Sci. Instrum.* **82** 103501

[24] Stangeby P.C. 2000 *The Plasma Boundary of Magnetic Fusion Devices* (Bristol: Institute of Physics)

[25] Faitsch M., Sieglin B., Eich T., Sun H.J. and Herrmann A. 2015 *Plasma Phys. Control. Fusion* **57** 075005

[26] Sun H.J., Wolfrum E., Eich T., Kurzan B., Potzel S. and Stroth U. 2015 *Plasma Phys. Control. Fusion* **57** 125011

[27] Silvagni D., Eich T., Faitsch M., Happel T., Sieglin B., David P., Nille D., Gil L. and Stroth U. 2020 *Plasma Phys. Control. Fusion* **62** 045015

[28] Fischer R., Fuchs C.J., Kurzan B., Suttrop W. and Wolfrum E. 2010 *Fusion Sci. Technol.* **58** 675

[29] Scott B.D. 2005 *Phys. Plasmas* **12** 062314

[30] Bonanomi N., Angioni C., Crandall P.C., Di Siena A., Maggi C.F. and Schneider P.A. 2019 *Nucl. Fusion* **59** 126025

[31] David P., Bernert M., Pütterich T., Fuchs C., Glöggler S. and Eich T. (The ASDEX Upgrade Team) 2021 *Nucl. Fusion* **61** 066025

[32] Cathey A., Hoelzl M., Harrer G., Dunne M.G., Huijsmans G.T.A., Lackner K., Pamela S.J.P., Wolfrum E. and Günter S. 2022 *Plasma Phys. Control. Fusion* **64** 054011

[33] Rogers B.N., Drake J.F. and Zeiler A. 1998 *Phys. Rev. Lett.* **81** 4396

[34] Labombard B., Hughes J.W., Mossessian D., Greenwald M., Lipschultz B. and Terry J.L. (The Alcator C-Mod Team) 2005 *Nucl. Fusion* **45** 1658

[35] Greenwald M. 2002 *Plasma Phys. Control. Fusion* **44** R27

[36] Eich T., Goldston R.J., Kallenbach A., Sieglin B. and Sun H.J. 2018 *Nucl. Fusion* **58** 034001

[37] Eich T. *et al* 2013 *Nucl. Fusion* **53** 093031

[38] Nille D. *et al* 2018 Probabilistic inference of surface heat flux densities from infrared thermography *Bayesian Inference and Maximum Entropy Methods in Science and Engineering* (Cham: Springer) pp 55–64

[39] Herrmann A., Junker W., Gunther K., Bosch S., Kaufmann M., Neuhauser J., Pautasso G., Richter T. and Schneider R. 1995 *Plasma Phys. Control. Fusion* **37** 17

[40] Eich T., Sieglin B., Scarabosio A., Fundamenski W., Goldston R.J. and Herrmann A. 2011 *Phys. Rev. Lett.* **107** 215001

[41] Giacomin M., Stagni A., Ricci P., Boedo J.A., Horacek J., Reimerdes H. and Tsui C.K. 2021 *Nucl. Fusion* **61** 076002

[42] Faitsch M., Maurizio R., Gallo A., Coda S., Eich T., Labit B., Merle A., Reimerdes H., Sieglin B. and Theiler C. 2018 *Plasma Phys. Control. Fusion* **60** 045010

[43] Dunne M.G. *et al* 2016 *Plasma Phys. Control. Fusion* **59** 025010

[44] Frassinetti L. *et al* 2019 *Nucl. Fusion* **59** 076038

[45] Siccinio M., Graves J.P., Kembleton R., Lux H., Maviglia F., Morris A.W., Morris J. and Zohm H. 2022 *Fusion Eng. Des.* **176** 113047

[46] Neu R. *et al* 2002 *Plasma Phys. Control. Fusion* **44** 811

[47] Eich T., Sieglin B., Thornton A.J., Faitsch M., Kirk A., Herrmann A. and Suttrop W. 2017 *Nucl. Mater. Energy* **12** 84

[48] Drenik A. *et al* 2019 *Nucl. Fusion* **59** 046010

[49] Lipschultz B., LaBombard B., Marmar E.S., Pickrell M.M., Terry J.L., Watterson R. and Wolfe S.M. 1984 *Nucl. Fusion* **24** 977

[50] Bernert M. *et al* 2014 *Plasma Phys. Control. Fusion* **57** 014038

[51] Maraschek M. *et al* 2017 *Plasma Phys. Control. Fusion* **60** 014047

[52] Pitts R. *et al* 2019 *Nucl. Mater. Energy* **20** 100696

[53] Chang C.S. *et al* 2017 *Nucl. Fusion* **57** 116023

[54] Sun H.J., Wolfrum E., Eich T., Kallenbach A., Schneider P., Kurzan B. and Stroth U. 2019 *Plasma Phys. Control. Fusion* **62** 025005

[55] Faitsch M., Eich T. and Sieglin B. 2020 *Plasma Phys. Control. Fusion* **62** 085004

[56] Redl A., Eich T., Vianello N. and David P. (The ASDEX Upgrade Team and The EUROfusion MST1 Team) 2023 *Nucl. Mater. Energy* **34** 101319